THE JOURNAL OF PHYSICAL CHEMISTRY C
A JOURNAL OF THE AMERICAN CHEMICAL SOCIETY

Extracting Bulk-like Semiconductor Parameters from the Characterization of Colloidal Quantum Dot Film Photoconductors

Published as part of The Journal of Physical Chemistry virtual special issue "Horst Weller Festschrift".

Philippe Guyot-Sionnest,* John C. Peterson, and Christopher Melnychuk

Cite This: https://doi.org/10.1021/acs.jpcc.2c05391 Read Online

ABSTRACT: A simple photoconductor structure based on a HgTe colloidal quantum dot (CQD) film on a field-effect transistor substrate is analyzed to provide quantitative information on the mobility, Fermi energy, and carrier number. Then, from the photocurrent with a calibrated light source and the optical constants of the materials, the carrier lifetime and recombination mechanism can be determined. The study confirms that geminate recombination is the dominant lifetime mechanism for these mid-infrared HgTe CQD films instead of trapping or Auger recombination. This work is a step toward answering the general question whether the individual properties of CQDs and their distribution in a film can be related to the simpler macroscopic optical and electrical properties of a homogeneous semiconductor.

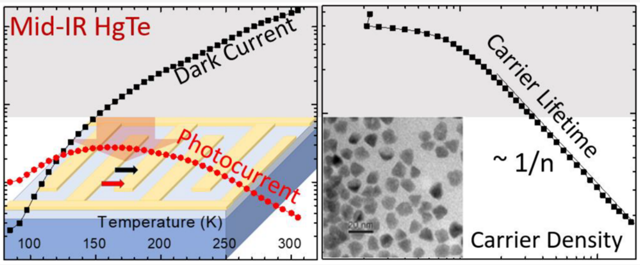

INTRODUCTION

A photoconductor is a simple device which requires the right wavelength of absorption, minimal nonradiative losses, and good charge transport properties. In principle, colloidal quantum dot (CQD) films and composites could allow for optimization of all these properties with greater ease than a bulk material. Research on CQD detectors is also an enticing academic topic as it builds upon many works and insights previously developed on these nanomaterials.

The facile tunability of the optical absorption with quantum confinement and composition was the starting point of colloidal quantum dots, demonstrated in the early 1980s by Ekimov and Efros, Brus, Henglein and Weller, and others.[1,2] Weller and co-workers used aqueous preparation and first introduced mercury ions in their studies of mixed CdS/HgS.[3] The subsequent aqueous synthesis of HgTe quantum dots by Rogach et al. led to the first CQDs in the near or short-wave infrared ($<2.5\ \mu$m).[4] The colloidal synthesis with organic solvents and organometallics pioneered by Steigerwald and Brus[5] became the dominant synthetic approach in the 1990s following the landmark work of Murray, Norris, and Bawendi[6] because it provides great control of temperature and surface chemistry. The organic solvent synthesis of PbSe[7] and PbS[8] was later developed and provided improved short-wave infrared spectral features. These lead chalcogenides were also synthesized using metal salts rather than toxic and pyrophoric organometallics, an approach that Peng generalized with CdX CQDs.[9] Kovalenko et al.[10] and Green et al.[11] inspired the later organic synthesis of widely tunable infrared HgTe CQDs starting with mercury salts.[12,13]

To allow efficient luminescence or charge extraction, passivation of ultrafast traps on the CQD surfaces is eminently required. In 1987, the Weller group introduced CdS nanocrystals passivated by cadmium hydroxide, which became the brightest stable colloidal quantum dot emitter.[14] Our first publication on CQDs in 1994 used these CdS/hydroxide nanocrystals to start the exploration of single CQD photoluminescence.[15] This was before the advent of CQDs core/shells synthesized in organic solvents,[16] which exceeded the brightness of the CdS/hydroxide. To date, passivation is still a topic of major importance for any CQDs, and it remains particularly challenging in the infrared.

Charge transport across nanocrystals is the third essential aspect of a CQD photoconductor. In the first photodetector investigation of CQDs, Wang and Herron used a conducting polymer to allow for CdS CQD photosensitizing.[17] This was because of the very insulating properties of the organic solvent-synthesized CQDs. CQDs synthesized in organic solvent continued to resist ohmic transport for many years.[18] In contrast, films of colloidal nanoparticles prepared in polar solvents exhibited better transport and phototransport properties after annealing.[19] Weller's group did pioneering work on

Received: July 29, 2022
Revised: September 18, 2022

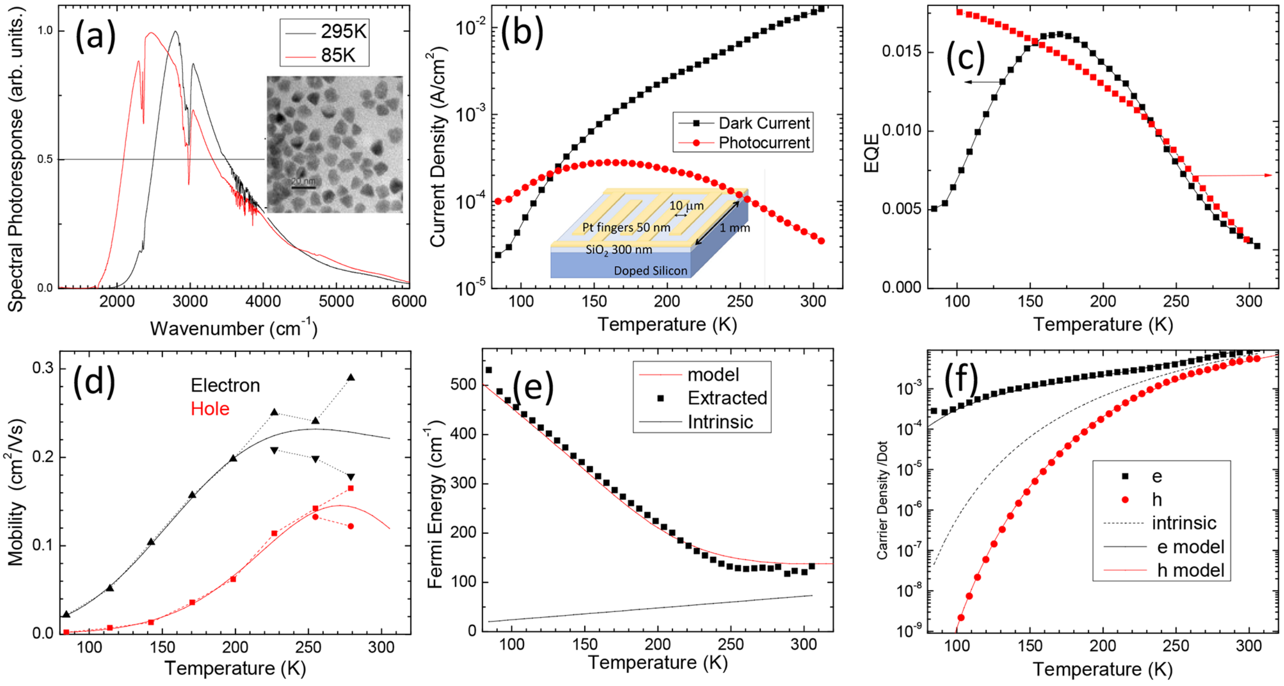

Figure 1. (a) Photocurrent spectra of the HgTe CQD films at 300 and 85 K. (b) Dark current density and photocurrent density. (c) EQE and detectivity. (d) Electron and hole mobility derived from FET measurements (e) Fermi energy of the sample (black symbols) extracted from the data analysis, and intrinsic Fermi energy (black line). The red line is a model described in the text. The energy scale is referenced to the midgap point. (f) Electron and hole number per dot derived from the Fermi energy in (e). The solid lines are from the modeled Fermi energy.

the conductivity and photoconductivity of such films of ZnO nanocrystals prepared from ethanol and aqueous solutions.[20] The work showed that it was the ZnO nanoparticle electrons that conducted the current, based in part from knowledge of the bulk polycrystalline ZnO as well as the Moss−Burstein blue-shift of the absorption edge under reducing conditions. This later led Vanmaekelbergh and co-workers to demonstrate state-resolved transport in ZnO nanocrystal films that were dried only at 90 °C.[21] HgTe CQD films using CQDs synthesized in aqueous solution directly with short and polar thioglycerol ligands and cast as films at room temperature also allowed photoresponse in the short-wave infrared.[22] It took the introduction of the solid state ligand exchange of organic capped quantum dots to achieve state-resolved ohmic conductivity with the more monodispersed CdSe CQD films,[23] and this opened up the route to efficient photodetector demonstrations with CdSe[24] and PbS CQDs.[25] Ligand exchange of organic capped CQDs by transfer to polar solution now allows much higher mobility[26] and improved photoresponse.[27]

Photodetector applications of CQDs require control over these three essential properties of absorption, passivation, and conduction. Ultimately, CQDs promise low cost and easy production in spectral ranges where silicon does not absorb light. The infrared is particularly attractive because infrared detectors and cameras are very useful but expensive. For imaging devices, wafers of infrared single-crystal epitaxial materials, which are not lattice matched to silicon, are mechanically bonded and connected pixel by pixel to the silicon-based read-out circuits. CQDs offer the simple alternative of solution processing by coating silicon chips with arbitrarily small pixels, at minimal costs. Compared to solution-processed organic molecules or polymers, the low phonon frequency of the inorganic CQD core should also not degrade the electronic energy as fast. The potential advantage of infrared CQDs is therefore very significant, and the challenge is to achieve relevant performances. The near-infrared (<1.3 μm) and short-wave infrared (1.3−2.5 μm) were first explored with PbS and HgTe CQDs. PbS CQDs cameras are now commercial and currently provide lower performance but potentially much lower cost for higher definition imaging than InGaAs. The mid-infrared, 3−5 μm, has many applications waiting for an affordable technology, including greenhouse gas imaging and passive thermal imaging of room temperature objects. The HgTe CQDs lead the mid-infrared efforts and performances are still being improved before commercial applications become viable.[28,29]

In parallel with ongoing experimentation with CQD synthesis, ligand exchange strategies, and device architecture, there is a need for basic research connecting the microscopic properties of the CQDs with the overall semiconducting properties of the CQD solid. A bulk semiconductor photodetector can be accurately modeled with a few parameters including the gap and effective masses, the optical constants, the carrier mobilities, and the carrier recombination rates and mechanisms (geminate, Auger, and Shockley−Read−Hall). It is still unknown to what degree variations of CQD properties allow a connection to such macroscopic properties. This article is in the line of prior work trying to map the behavior of CQD films to those of semiconductors.[30−35] It discusses a limited set of simple optical, electrical, and photoresponse measurements on HgTe CQDs, and a rather successful attempt to extract semiconductor properties and model the photoresponse.

■ METHODS

The system studied is a film of mid-IR HgTe CQDs deposited on interdigitated electrodes. The nonaggregated HgTe CQDs are synthesized following Lan and co-workers.[36] A TEM image of the HgTe CQDs is shown as an inset in Figure 1a. The substrate is an interdigitated Pt electrode with a gap of $L = 10$ μm, evaporated on 300 nm of SiO_2 on doped Si. A schematic is shown in Figure 1b. There are 25 pairs of interdigitated fingers of 1 mm length corresponding to a total channel width of $W = 4.9$ cm. The CQD/chlorobenzene solution is drop-cast in air at 40 °C as a single layer, and the film is cross-linked with a solution of 1:1:50 ethanedithiol/HCl/isopropanol by volume. Laser profilometry indicates that the film thickness is ~100 nm. The film is then sealed by spin-coating a ~800 nm layer of PMMA and dried in air at 80 °C for 3 min.

The spectral photoresponse is measured by using the photoconductor as an external detector to a Nicolet 550 Fourier Transform Infrared Spectrometer. The photoconductor is biased and the current is amplified by a FemtoDLPCA-200 current amplifier followed by a SRS560 voltage amplifier. The noise is measured by a SR760 spectrum analyzer. A calibrated light source is provided by a blackbody source, Omega BB-4A, at 600 °C, of 21 mm diameter, and placed 15 cm from the sample. The sample is mounted in a cryostat with a CaF_2 window and cooled with liquid nitrogen. Data as a function of temperature are measured as the cryostat is warmed up. Field-effect transistor measurements are performed on the same samples.

■ RESULTS AND DISCUSSION

Model. The photoconductor is modeled as a semiconductor with a uniform doping level and thickness. The photocurrent is given by

$$I = \alpha\eta\phi\, \tau(\mu_e + \mu_p)(LW)\, \frac{eV}{L^2} \tag{1}$$

α is the optical absorption of the film, η is the probability of ionizing the created exciton into separate electrons and holes, ϕ is the photon flux ($1/\mathrm{cm}^2$ s), τ is the carrier lifetime, μ_e and μ_h are the electron mobility and hole mobility respectively, e is the elementary charge, and V is the applied bias. The photoconductor device width is W, and L is the length of the conducting channel. The dark current is expressed as

$$I_0 = (n_0\mu_e + p_0\mu_p)\left(\frac{LWd}{V_{\mathrm{dot}}}\right)\frac{eV}{L^2} \tag{2}$$

where n_0 and p_0 are respectively the unitless density of mobile electrons and holes per dot. The film thickness is d, and V_{dot} is the effective volume of the dot, including the dot and void volumes.

The carrier lifetime in eq 1 is related to the recombination mechanism within a dot by assuming that electrons and holes diffuse though the film of dots, and that recombination can only take place within a dot. The rate of disappearance of electrons is given

$$\frac{\mathrm{d}n}{\mathrm{d}t} = -\frac{np}{\tau} + G_{\mathrm{th}} = \frac{\mathrm{d}p}{\mathrm{d}t} \tag{3}$$

where the carrier densities are normalized per dot as above, G_{th} is the generation rate, and τ^{-1} is the recombination rate. Writing $n = \delta n + n_0$ and $p = \delta p + p_0$, where n_0 and p_0 are the equilibrium values. Charge neutrality requires $\delta n = \delta p$. The thermal generation rate is then $G_{\mathrm{th}} = \frac{n_0 p_0}{\tau}$ as required for equilibrium. The carrier lifetime can be further related to microscopic recombination mechanisms. We distinguish the following cases: (i) A dot with an electron and a positive trap with a probability nn_{t+}, and the electron is trapped with a decay time τ_{t+}. A symmetric case exists for hole and a negative trap. (ii) A dot with an electron and a hole with probability np, an electron and a hole decay in τ_{exc}, which is the excitonic lifetime related to the lifetime measured for isolated dots. (iii) A dot with 2 electrons and a hole, with a probability $2n^2p$, and an electron and a hole decay in $\tau_{\mathrm{A,ccv}}$. (iv) A dot with one electron and two holes, with probability $2np^2$, and an electron and a hole decay in $\tau_{\mathrm{A,cvv}}$.

These few cases should be sufficient to capture the situation of low carrier densities. The overall rate of change of the electron density will depend on the relative rate of hopping and the decay time.

If the hopping time is much faster than the decay times, then the overall population decay is

$$\frac{\mathrm{d}n}{\mathrm{d}t} = G_{\mathrm{th}} - \frac{pn}{\tau_{\mathrm{exc}}} - \frac{nn_{t+}}{\tau_{t+}} - \frac{2n^2p}{\tau_{\mathrm{A,ccv}}} - \frac{2np^2}{\tau_{\mathrm{A,cvv}}} \tag{4}$$

The same expression applies for the holes, such that the number $n + p + n_{t+} + n_{t-}$ is constant as required by charge neutrality. Then, we use the equilibrium to determine that $G_{\mathrm{th}} = \frac{p_0 n_0}{\tau_{\mathrm{exc}}} + \frac{n_0 n_{t+}}{\tau_{t+}} + \frac{2{n_0}^2 p_0}{\tau_{\mathrm{A,ccv}}} + \frac{2n_0{p_0}^2}{\tau_{\mathrm{A,cvv}}}$, so $\frac{\mathrm{d}\delta n}{\mathrm{d}t} = -\frac{\delta n(n_0 + p_0)}{\tau_{\mathrm{exc}}} - \frac{\delta n n_{t+}}{\tau_{t+}} - 6\delta n n_0 p_0\left(\frac{1}{\tau_{\mathrm{A,ccv}}} + \frac{1}{\tau_{\mathrm{A,cvv}}}\right) - \ldots$ This allows one to relate the microscopic lifetimes to the carrier lifetime in the conducting CQD film.

For geminate recombination, the carrier lifetime is

$$\tau^{-1} = \frac{n_0 + p_0}{\tau_{\mathrm{exc}}} \tag{5}$$

For trapping, τ^{-1} is independent of carrier concentration, with $\tau^{-1} = \frac{n_t}{\tau_t}$. For Auger, $\tau^{-1} = 6{n_i}^2\frac{1}{\tau_A}$ where $n_i = \sqrt{n_0 p_0}$. This differs from the expression ${n_i}^2\frac{1}{8\tau_A}$ proposed by others.[37]

If the hopping time is slow compared to the decay times within a dot, the lifetimes in eq 4 should be replaced by the hopping time. With mobilities in the 0.01–0.3 $\mathrm{cm}^2/(\mathrm{V\ s})$ and center to center dot separation of $2r = 12$ nm, the calculated hopping time, $\tau_{\mathrm{hop}} = \frac{e(2r)^2}{6k_B T\mu}$, varies from 1.5 ns to 42 ps, respectively, from 85 to 300 K. These times are shorter than the exciton nonradiative lifetimes and the Auger times at room temperature, but they are likely to be much longer than the trapping time at all temperatures. Therefore, for trapping, the rate is limited by hopping and should instead be taken as $\tau^{-1} = \frac{n_t}{\tau_{\mathrm{hop}}}$.

Photoconductor Characterization. The spectral photoresponse is measured to determine the energy band gap, and it is shown in Figure 1a. The photoresponse edge has a finite width, of about 500 cm^{-1} from 10 to 90% of the edge. This introduces uncertainty on the band gap which is defined as the 1/2-point on the rising edge. The band gap red-shifts upon cooling, and for mid-IR HgTe CQD sizes, it shifts approximately linearly with temperature.[38] For this sample, the gap is 2500 cm^{-1} at $T = 295$ K and 2100 cm^{-1} at $T = 85$ K, and the band gap in cm^{-1} is modeled as $\nu_0 = 1940 + 1.9T$. The response speed is verified to be faster than 50 kHz by comparing interferograms at different scan rates. The dark current and photocurrent are measured as a function of

https://doi.org/10.1021/acs.jpcc.2c05391
J. Phys. Chem. C XXXX, XXX, XXX−XXX

temperature as shown in Figure 1b. On the log scale, it is apparent that the fractional decrease of the dark current upon cooling is accompanied by a similar fractional increase of the photocurrent. This is a significant observation that will be assigned to the reduction of the carrier density.

The responsivity (A/W) and the external quantum efficiency (EQE) are related by $\mathcal{R} = \mathrm{EQE}\frac{e}{h\nu}$ They are determined by using a blackbody source of defined area, temperature, and distance from the sample. The gap determined earlier is used to integrate the input photon flux from the blackbody. The root-mean-square (rms) noise current at 500 Hz in a 1 Hz bandwidth, i_n, is measured to provide the detectivity as $\mathcal{D}^* = \frac{\mathcal{R}}{i_n}A^{1/2}$ (cm W^{-1} $\mathrm{Hz}^{-1/2}$ or Jones) where A is the total area of the device within the electrodes. EQE and detectivity are shown in Figure 1c. The low EQE is due to the small optical absorption of ∼10% and the shorter drift length compared to the 10 μm electrode gap, as will be discussed later. The detectivity of the 100 nm thin sample at 295 K is 1×10^8 Jones which is only 2-fold lower than prior results with photovoltaic films of 400 nm thickness.[39] It is slightly higher than previous photoconductor devices with high mobility transport,[40] and it is therefore a fair device at room temperature. However, at 85K, the detectivity is only 5×10^9 Jones which is more than 10-fold worse than with photovoltaic HgTe devices. The reason is that the film is not close enough to intrinsic as will be shown later.

Carrier Mobility Determination. The mobilities of the electron and hole are determined as a function of temperature by scanning a gate voltage to the underlying doped Si substrate.[41] The source−drain currents are measured with forward and backward gate scanning between +30 and −30 V, and the values of the steepest slope are used to determine the mobility. The data are shown in Figure 1d, and the mobilities are fitted to a smooth third order polynomial expression. Mobilities determined by FET carry some uncertainties and the steepest slopes of the FET source−drain curve may not reflect the actual mobility of photocarriers. Above ∼200 K, the FET source−drain current has a hysteresis with gate voltage scan direction as shown in Figure S1. We assign the effect to the diffusion of ions that neutralize the gate charges. This leads to two values for the mobility shown in Figure 1d. Another uncertainty of FET measurements is that the measured mobility for electrons and holes depends on the background doping, and this has been attributed to additional scattering of the carriers in the gated layer due to the presence of the opposite charge carriers above the gated layer.[39] Therefore, the FET mobility in these nearly intrinsic films may be lower than the photocarrier mobilities and future comparison with other mobility measurements will be needed.

Fermi Energy and Carrier Density Determination. Knowing the dark current, the mobility, and the sign of the doping, we determine the Fermi energy and carrier density using eq 2. For this sample, the FET measurement showed that it was slightly n-type. Taking the midgap as the zero of energy, the electron density per dot is modeled as

$$n_0 = N_c/\left(1 + \exp\left(\frac{E_g/2 - E_f}{k_B T}\right)\right) \sim N_c \exp\left(\frac{-E_g/2 + E_f}{k_B T}\right)$$

The hole density is similarly $p_0 \sim N_v \exp\left(\frac{-E_g/2 - E_f}{k_B T}\right)$. N_c and N_v are constants that reflect the number of thermally accessible conduction and valence states, respectively. Calling $x = \mathrm{e}^{E_f/k_B T}$, the dark current is then

$$I_0 = \left(N_c\,\mathrm{e}^{-E_g/2k_B T}\,\mu_e x + N_v\,\mathrm{e}^{-E_g/2k_B T}\,\mu_p \frac{1}{x}\right)\left(\frac{LWd}{V_{\mathrm{dot}}}\right)\frac{eV}{L^2} \tag{6}$$

The solution to this quadratic equation is

$$x = \frac{I_0/\left[\left(\frac{LWd}{V_{\mathrm{dot}}}\right)\frac{eV}{L^2}\right] \pm \sqrt{\left(I_0/\left[\left(\frac{LWd}{V_{\mathrm{dot}}}\right)\frac{eV}{L^2}\right]\right)^2 - 4N_c N_v\,\mathrm{e}^{-E_g/k_B T}\mu_e\mu_p}}{2N_c\,\mathrm{e}^{-E_g/2k_B T}\,\mu_e} \tag{7}$$

and the Fermi energy is $E_f = k_B T \ln(x)$. Of the two solutions, the correct one is such that the Fermi energy corresponds to the n-doping of the sample. The quantity $\left(\frac{LWd}{V_{\mathrm{dot}}}\right)$ is the number of CQDs in the device and this is prone to error, easily as much as a factor of 2 due to size and packing uncertainty. Nevertheless, at the higher temperature the CQD film should be dominated by its intrinsic behavior and the Fermi energy should be close to the intrinsic value of $\frac{k_B T}{2}\ln(N_v/N_c)$. This constrains the quantity $\left[\left(\frac{d}{V_{\mathrm{dot}}}\right)\frac{eV}{L^2}\right]$ to ∼5 ± 1 $\mathrm{J/cm^4}$ when taking $N_c = 2$ (doubly degenerate $1S_e$ state) and $N_v = 4$ (approximate number of populated hole states in this temperature range).[33] With $d \sim 100$ nm, $V = 0.33$ V, and $L = 10$ mm, this gives $V_{\mathrm{dot}} = 1.06 \times 10^{-20}$ cm^3. This is the volume of a cube of 5.8 nm edge length or a tetrahedron of 11.2 nm edge length which is close to the dot size but leaves no room for void space. We would therefore expect a V_{dot} about 2-fold larger. Sources of errors could be an underestimate of the thickness d due to inhomogeneity over the mm^2 device or an overestimate of the length L due to imprecision in the lithography. The extracted Fermi energy is shown in Figure 1e. It is close to the intrinsic value at room temperature by choice of $\left[\left(\frac{d}{V_{\mathrm{dot}}}\right)\frac{eV}{L^2}\right]$, but it also shows an increase with decreasing temperature. The number of electrons and holes per dot determined from the Fermi energy are shown in Figure 1f. For this sample, the imbalance between electrons and holes becomes significant below 200 K. The doping is n-type and about 3×10^{-4}/dot at 85 K, compared to an essentially thermal doping of 10^{-2}/dot at 300 K. Thus, although this sample provides a good photoresponse and detectivity at room temperature, it is too far from intrinsic to be a good photodetector at low temperature. The deviation from intrinsic is dependent on sample preparation and on exposure to air, the latter gradually moving the doping p-type. This illustrates the difficulty in using the mid-IR HgTe CQDs in photoconducting devices for low temperature operation, where the doping needs to be stable and less than 10^{-5} e/dot in order to reduce the dark current and reach background-limited performance.

The Fermi energy is consistent with neither a fixed value nor a model of shallow donors or acceptors. Figure 1e,f shows that a fair rendition of the Fermi energy and carrier density is obtained by assuming that the Fermi energy arises from equilibrium between 4 valence hole states, 2 conduction electron states, and a small density of midgap donors, 4×10^{-3}/dot, for a total of 4.004 electrons distributed over 6.004 states. More work will be needed to identify such a small

https://doi.org/10.1021/acs.jpcc.2c05391
J. Phys. Chem. C XXXX, XXX, XXX−XXX

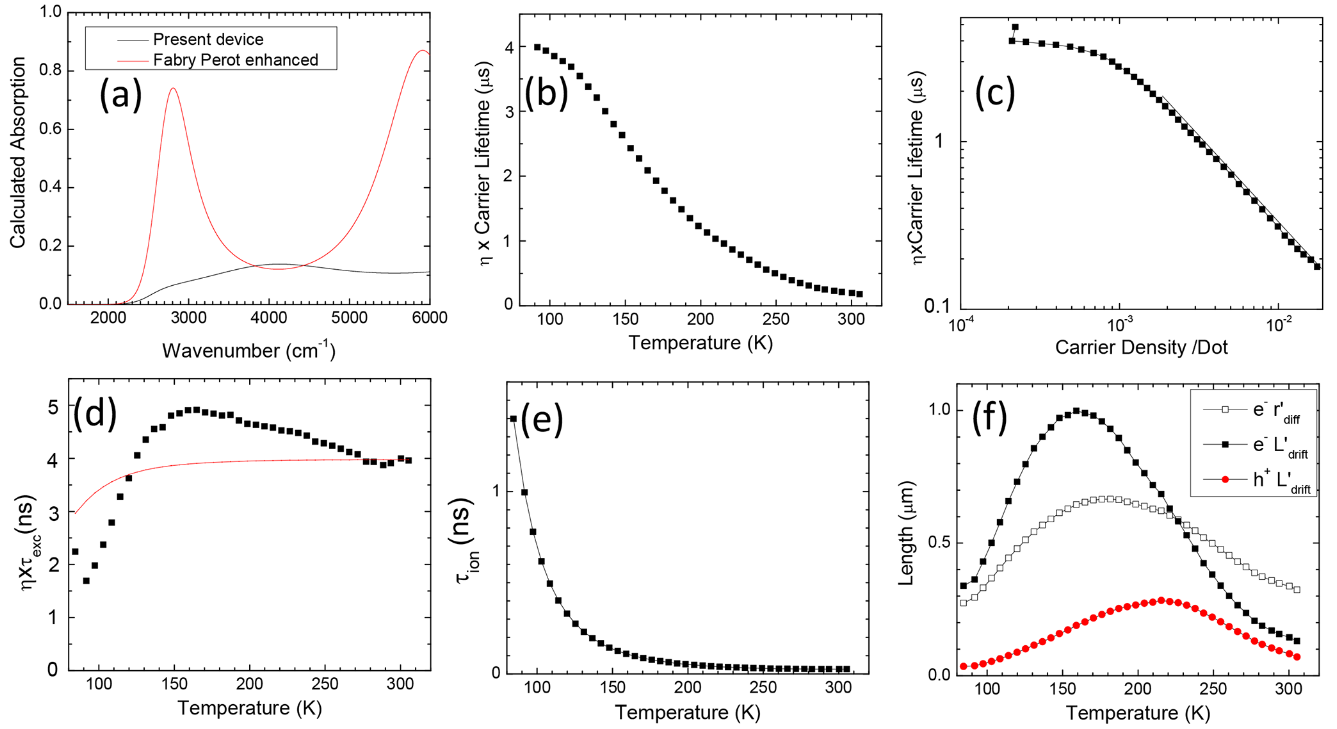

Figure 2. (a) Calculated optical absorption for the 100 nm thick HgTe sample in this study, and for a proposed enhanced device with 600 nm thick HgTe as described below. (b) Extracted product of carrier lifetime and ionization efficiency. (c) Same result as a function of the carrier concentration, the solid line has a slope of −1. (d) Extracted product of excitonic lifetime and ionization efficiency. The red line is for a fixed 4 ns excitonic lifetime and a temperature dependent ionization efficiency (e) Calculated ionization time. (f) Calculated electron and hole drift lengths with 0.3 V bias, and calculated diffusion length for the electron.

density of midgap states and explore their possible relation to trapping.

Carrier Lifetime. The carrier lifetime is extracted from analyzing the photocurrent, starting with an estimation of the photon flux absorbed $\alpha\phi(LW)$ in eq 1. For this purpose, the index of refraction of the CQD film is determined by fitting a transmission measurement of a film of measured thickness on a ZnSe plate. From 1000 to 6000 cm^{-1} a good fit is obtained with an index of refraction $n + \frac{ik}{e^{(\nu-\nu_0)/\Delta\nu}+1}$ with $n = 2.25$, $k = 0.13$, ν_0 being the band gap defined earlier, and $\Delta\nu = 110$ cm^{-1} (Figure S2). k is slightly higher than the value of 0.1 used in earlier simulations[39] and identical to a later report,[42] both using the "aggregated" HgTe CQDs preparation developed by Keuleyan et al.[43] This expression does not satisfy the Kramers−Kronig relation and the estimated uncertainty is 0.1 for n and 0.01 for k. Using the photoconductor sample film thickness of ∼100 nm, the material stack, and a 1D transfer matrix program, the absorption of the photoconductor film is calculated and shown in Figure 2a. The blackbody spectrum, the temperature of the blackbody and its area and distance from the sample provide the absorbed photon flux $\alpha\phi$, calculated as a function of sample temperature. From the photocurrent and the carrier mobility, the quantity $\eta\tau$ is then determined as a function of temperature and shown in Figure 2b. This product increases from 300 ns at 295 K to 4 μs at 85K. These times are much longer than any transient times measured in isolated HgTe CQDs because the ionized carriers need to travel some distance before recombination.

The product $\eta\tau$ as a function of carrier number per dot is shown in Figure 2c, and this shows an approximately inverse linear relation with the carrier concentration. This is a strong indication that the lifetime is due to geminate recombination. In contrast, a trap limited lifetime would be constant, and an Auger-limited lifetime would have a slope of −2. Moreover, using the Auger biexciton lifetime $\tau_A > 100$ ps previously determined for mid-IR HgTe CQDs,[44] the estimated carrier lifetime from Auger, $\tau^{-1} = 6n_i^2\frac{1}{\tau_A}$, is slower than the measured carrier lifetime in Figure 2b at all temperatures, in agreement with earlier modeling.[33]

A lifetime dominated by geminate carrier recombination had been assumed previously for mid-IR HgTe films,[33,40] and this analysis justifies the assumption at least near room temperature.

This is further conveyed by calculating a hypothetical excitonic lifetime using $\tau^{-1} = \frac{n_0+p_0}{\tau_{exc}}$, shown in Figure 2d. The nearly constant value of $\eta\tau_{exc}$ down to 150 K supports the hypothesis that geminate recombination limits the lifetime. Assuming a unity ionization efficiency above 150 K, $\tau_{exc} \sim 4$ ns. This value is about 5-fold longer than reported transient absorption lifetimes in solution.[44] It appears to be a bit large for the ∼10^{-3} quantum efficiency of photoluminescence of the HgTe films but a detailed analysis will require accounting for the photon extraction. The weak temperature dependence of τ_{exc} down to 150 K is consistent with the weak temperature effect on the PL efficiency for such films. Figure.S3 shows overall rather similar results for a film of "aggregated" HgTe CQD synthesized according to ref 43. It also shows a different behavior after aging in air for a week, and this is tentatively assigned to the growing influence of carrier trapping.

Below 150 K, the $\eta\tau$ product plateaus and this could be due to the rising importance of trapping. Trapping in CQDs is usually fast, on a picosecond time scale such that trapping is limited by the rate at which the carriers sample the quantum dots, leading to a trapping lifetime given by $\tau^{-1} = \frac{n_t}{\tau_{\text{hop}}}$ as discussed earlier. By fitting the measured lifetime to two terms, $\tau^{-1} = \frac{n_0 + p_0}{\tau_{\text{exc}}(T)} + \frac{n_t}{\tau_{\text{hop}}}$, and assuming a linear temperature dependence of $\tau_{\text{exc}}(T)$, a maximum density of electron or hole trapping sites is determined, reaching at most 10^{-3}/dot at low temperature (Figure S4). The larger density of thermal carriers in mid-IR CQDs helps ensure that recombination with thermal carriers dominates at room temperature, while traps are more readily relevant for short-wave IR CQD films.[31] Besides trapping, an alternative explanation for the plateau of $\eta\tau$ at low temperature is a reduction of the ionization efficiency. The time for ionization is taken as $\tau_{\text{ion}} = \frac{1}{(\tau_{\text{hop,e}}^{-1} + \tau_{\text{hop,h}}^{-1})} = \frac{e(2r)^2}{6k_BT(\mu_e + \mu_h)}$ where $2r$ is the interdot center to center distance of roughly 12 nm. As shown in Figure 2e, this time increases to about 1.5 ns at 85 K which starts to compete with τ_{exc}. Calculating an ionization efficiency as $\eta = \frac{\tau_{\text{ion}}^{-1}}{\tau_{\text{exc}}^{-1} + \tau_{\text{ion}}^{-1}}$ only accounts for half of the observed lifetime saturation, but this is fair given the approximations made in this work.

The analysis above helps explains why the EQE shown in Figure 1c is in the 1% range, while the absorption is ~10%. At room temperature, we expect $\eta \sim 1$, and the drift lengths are expected to be close to $L'_{\text{drift}} = \eta\tau\mu_{\text{e,h}}\frac{V}{L}$ and shown in Figure 2f. By their definition, these lengths have a similar temperature dependence as the EQE. Figure 2f shows that they are less than 1 μm with the 0.3 V bias. This is 10-fold shorter than the electrode channel length, justifying the use of eqs 1 and 2 and explaining the 1% EQE. Figure 2f also shows a calculated electron diffusion length as $r'_{\text{diff}} = \sqrt{\frac{k_BT\eta\tau\mu_e}{e}}$. Upon cooling from room temperature, the lengths increase because longer carrier lifetimes more than compensate for reduced mobility. At low temperature, the calculated lengths are only minimal values as n becomes less than unity.

Using the Previous Information to Design a Better Device. Simplifying eq 1 and 2 by considering one carrier, the photocurrent is $I = \alpha\eta\phi A\tau\mu\frac{eV}{L^2}$ where A is the detector area and L is the channel length. The dark current is $I_0 = n_0\left(\frac{Ad}{V_{\text{dot}}}\right)\mu\frac{eV}{L^2}$ where d is the film thickness. At 500 Hz, the room temperature noise for the sample studied here was 6 pAHz$^{-1/2}$ for a dark current of 71 μA, already close to the calculated shot noise, $i_n = \sqrt{2eI_0}$, and the $1/f$ noise decreased at low temperatures. Using the shot noise gives the detectivity as

$$\text{D}^* = \frac{1}{h\nu}\frac{\alpha}{\sqrt{d}}\eta\tau\sqrt{\mu\frac{V}{L^2}\frac{V_{\text{dot}}}{2n_0}} \tag{8}$$

The prior discussion showed that a unity photoionization is expected at room temperature so that $\eta = 1$. The device discussed above had an absorption α = 10%, and a thickness d ~ 100 nm. The mobility was 0.3 cm^2/(V s), the bias was 0.3 V and L = 10 μm. At room temperature, the measured carrier lifetime was 300 ns with the carrier concentration ~0.01 e/dot. With these numbers the room temperature detectivity is calculated to be 1.5 × 10^8 Jones which matches the experimental value in Figure 1c. The carrier collection efficiency can be improved by raising the bias or narrowing the device. Since raising the bias leads to increasing $1/f$ noise, the better option is to reduce the gap length L, which can be done using very narrow gap electrodes made by e-beam lithography[45] or using a sandwiched structure similar to previous PV structures.[39] The latter can also increase the absorption while matching the drift length to the thickness which is now such that $d = L$. Using a semitransparent top electrode of 3 nm Au, a 600 nm thick film of CQDs, and a bottom Au electrode of 50 nm, the absorption is calculated to be ~70% as shown in Figure 2a. The bias is chosen such that $\mu\frac{V}{L^2} = \tau^{-1}$, as this matches the drift length to the device thickness. With L = 600 nm, the measured carrier lifetime and mobility at room temperature, the bias needs to be 40 mV and small enough that the $1/f$ noise will not increase significantly. While it may be challenging to make such thin metal electrodes with smooth topography and high conductivity, the expected detectivity of this proposed device would be 2.7 × 10^9 Jones at room temperature. This is still less than commercial PbSe detector, but it is better than pyroelectric and microbolometers and allows a microsecond response. With appropriately intrinsic doping, the low temperature detectivity can be similarly improved. As previously emphasized,[29,33] greater improvements will be possible by increasing the excitonic lifetime, and this will require understanding and overcoming the nonradiative recombination in the mid-IR.

■ CONCLUSION

The possibility of detecting thermal photons with colloidal quantum dots could not have been envisioned in the early days of CQDs. Since then, knowledge has greatly increased, and thermal infrared detection is one of the numerous realistic applications of CQDs. Advances still require the basic understanding of many properties so that CQD solids might advantageously replace bulk semiconductors. This work demonstrates that a few measurements on a simple photoconductor structure based on a HgTe CQD film provide a wealth of quantitative information. Using the measured mobilities of the electrons and holes as functions of temperature and the measured dark current, the carrier concentrations and the Fermi energy are obtained. Then, from the photocurrent with a calibrated light source and the optical constant of the material, the carrier lifetime and recombination mechanism can be determined. The data show that geminate recombination is the dominant mechanism for this mid-infrared HgTe CQD film in the range of 150−300 K. The data also provide drift and diffusion lengths and allow for modeling the detectivity.

The simple measurements and analysis will allow screening of CQD systems, by separating the effects of carrier density and lifetime which are typically lumped together when only reporting quantum efficiency or detectivity. This characterization can then be refined to improve the accuracy of the extracted properties, by separate measurements of photoluminescence quantum yield, absorption and photoluminescence transients, electrical transient photoconductivity, and time-of-flight. This work is a step toward answering the general question whether the individual properties of CQDs and their distribution can be related to the macroscopic optical and electrical properties of the CQD films.

■ ASSOCIATED CONTENT

Supporting Information

The Supporting Information is available free of charge at https://pubs.acs.org/doi/10.1021/acs.jpcc.2c05391.

> FET data of the sample described in the main text, determination of film optical constant, similar measurements taken on a "aggregated" HgTe CQD sample with the same energy gap as the sample in the main text, tentative evaluation of trapping density for the sample described in the main text (PDF)

■ AUTHOR INFORMATION

Corresponding Author

Philippe Guyot-Sionnest − *James Franck Institute, The University of Chicago, Chicago, Illinois 60637, United States;* orcid.org/0000-0003-0178-6255; Email: pgs@uchicago.edu

Authors

John C. Peterson − *James Franck Institute, The University of Chicago, Chicago, Illinois 60637, United States;* orcid.org/0000-0002-0509-6959

Christopher Melnychuk − *James Franck Institute, The University of Chicago, Chicago, Illinois 60637, United States;* orcid.org/0000-0003-4503-4135

Complete contact information is available at: https://pubs.acs.org/10.1021/acs.jpcc.2c05391

Notes

The authors declare no competing financial interest.

■ ACKNOWLEDGMENTS

This work was supported by ONR grant N00014-22-1-2027.

■ REFERENCES

(1) Efros, A. L.; Brus, L. E. Nanocrystal Quantum Dots: From Discovery to Modern Development. *ACS Nano* **2021**, *15*, 6192−6210.

(2) Weller, H.; Koch, U.; Gutierrez, M.; Henglein, A. Photochemistry of colloidal metal sulfides. 7. Absorption and fluorescence of extremely small ZnS particles (the world of the neglected dimensions). *Berichte der Bunsengesellschaft für Physikalische Chemie* **1984**, *88* (7), 649−656.

(3) Hasselbarth, A.; Eychmuller, A.; Eichberger, R.; Giersig, M.; Mews, A.; Weller, H. Chemistry and photophysics of mixed CdS/HgS colloids. *J. Phys. Chem.* **1993**, *97* (20), 5333−5340.

(4) Rogach, A.; Kershaw, S. V.; Burt, M.; Harrison, M. T.; Kornowski, A.; Eychmüller, A.; Weller, H. Colloidally prepared HgTe nanocrystals with strong room-temperature infrared luminescence. *Adv. Mater.* **1999**, *11*, 552−555.

(5) Steigerwald, M. L.; Brus, L. E. Synthesis, stabilization, and electronic structure of quantum semiconductor nanoclusters. *Annu. Rev. Mater. Sci.* **1989**, *19* (1), 471−495.

(6) Murray, C. B.; Norris, D. J.; Bawendi, M. G. Synthesis and characterization of nearly monodisperse CdE (E= sulfur, selenium, tellurium) semiconductor nanocrystallites. *J. Am. Chem. Soc.* **1993**, *115* (19), 8706−8715.

(7) Murray, C. B.; Sun, S.; Gaschler, W.; Doyle, H.; Betley, T. A.; Kagan, C. R. Colloidal synthesis of nanocrystals and nanocrystals superlattices. *IBM J. Res. Dev.* **2001**, *45*, 47−56.

(8) Hines, M. A.; Scholes, G. D. Colloidal PbS nanocrystals with size-tunable near-infrared emission: observation of post-synthesis self-narrowing of the particle size distribution. *Adv. Mater.* **2003**, *15* (21), 1844−1849.

(9) Peng, Z. A.; Peng, X. Formation of high-quality CdTe, CdSe, and CdS nanocrystals using CdO as precursor. *J. Am. Chem. Soc.* **2001**, *123* (1), 183−184.

(10) Kovalenko, M. V.; Kaufmann, E.; Pachinger, D.; Roither, J.; Huber, M.; Stangl, J.; Hesser, G.; Schäffler, F.; Heiss, W. Colloidal HgTe Nanocrystals with Widely Tunable Narrow Band Gap Energies: From Telecommunications to Molecular Vibrations. *J. Am. Chem. Soc.* **2006**, *128* (11), 3516−3517.

(11) Green, M.; Wakefield, G.; Dobson, P. J. A simple metalorganic route to organically passivated mercury telluride nanocrystals. *J. Mater. Chem.* **2003**, *13*, 1076−1078.

(12) Keuleyan, S.; Lhuillier, E.; Guyot-Sionnest, P. Synthesis of colloidal HgTe quantum dots for narrow mid-IR emission and detection. *J. Am. Chem. Soc.* **2011**, *133*, 16422−16424.

(13) Goubet, N.; Jagtap, A.; Livache, C.; Martinez, B.; Portalès, H.; Xu, X. Z.; Lobo, R. P. S. M.; Dubertret, B.; Lhuillier, E. Terahertz HgTe nanocrystals: beyond confinement. *J. Am. Chem. Soc.* **2018**, *140*, 5033−5036.

(14) Spanhel, L.; Haase, M.; Weller, H.; Henglein, A. Photochemistry of colloidal semiconductors. 20. Surface modification and stability of strong luminescing CdS particles. *J. Am. Chem. Soc.* **1987**, *109*, 5649−5655.

(15) Blanton, S. A.; Dehestani, A.; Lin, P. C.; Guyot-Sionnest, P. Photoluminescence of single semiconductor nanocrystallites by two-photon excitation microscopy. *Chemical physics letters* **1994**, *229* (3), 317−322.

(16) Hines, M. A.; Guyot-Sionnest, P. Synthesis and characterization of strongly luminescing ZnS-capped CdSe nanocrystals. *J. Phys. Chem.* **1996**, *100*, 468−71.

(17) Wang, Y.; Herron, N. Photoconductivity of CdS nanocluster-doped polymers. *Chem. Phys. Lett.* **1992**, *200*, 71−75.

(18) Ginger, D. S.; Greenham, N. C. Charge transport in semiconductor nanocrystals. *Synthetic metals* **2001**, *124*, 117−120.

(19) Hotchandani, S.; Kamat, P. V. Modification of electrode surface with semiconductor colloids and its sensitization with chlorophyll. *Chem. Phys. Lett.* **1992**, *191*, 320−326.

(20) Hoyer, P.; Eichberger, R.; Weller, H. Spectroelectrochemical investigations of nanocrystalline ZnO films. *Berichte der Bunsengesellschaft für physikalische Chemie* **1993**, *97*, 630−635.

(21) Roest, A. L.; Kelly, J. J.; Vanmaekelbergh, D.; Meulenkamp, E. A. Staircase in the electron mobility of a ZnO quantum dot assembly due to shell filling. *Physical review letters* **2002**, *89* (3), 036801.

(22) Kim, H.; Cho, K.; Song, H.; Min, B.; Lee, J. S.; Kim, G. T.; Kim, S.; Kim, S. H.; Noh, T. Photocurrent mechanism in a hybrid systems of 1-thioglycerol capped HgTe nanoparticles. *Appl. Phys. Lett.* **2003**, *83*, 4619−4621.

(23) Yu, D.; Wang, C.; Guyot-Sionnest, P. n-Type conducting CdSe nanocrystal solids. *Science* **2003**, *300* (5623), 1277−1280.

(24) Oertel, D. C.; Bawendi, M. G.; Arango, A. C.; Bulovic, V. Photodetectors based on treated CdSe quantum-dot films. *Appl. Phys. Lett.* **2005**, *87*, 213505.

(25) Konstantatos, G.; Howard, I.; Fischer, A.; Hoogland, S.; Clifford, J.; Klem, E.; Levina, L.; Sargent, E. H. Ultrasensitive solution-cast quantum dot photodetectors. *Nature* **2006**, *442*, 180−183.

(26) Kovalenko, M. V.; Scheele, M.; Talapin, D. V. Colloidal nanocrystals with molecular metal chalcogenide surface ligands. *Science* **2009**, *324* (5933), 1417−1420.

(27) Tang, J.; Kemp, K. W.; Hoogland, S.; Jeong, K. S.; Liu, H.; Levina, L.; Furukawa, M.; Wang, X.; Debnath, R.; Cha, D.; et al. Colloidal-quantum-dot photovoltaics using atomic-ligand passivation. *Nature materials* **2011**, *10*, 765−771.

(28) Keuleyan, S.; Lhuillier, E.; Brajuskovic, V.; Guyot-Sionnest, P. Mid-infrared HgTe colloidal quantum dot photodetectors. *Nat. Photonics* **2011**, *5* (8), 489−493.

(29) Guyot-Sionnest, P.; Ackerman, M. M.; Tang, X. Colloidal quantum dots for infrared detection beyond silicon, The. *J. Chem. Phys.* **2019**, *151* (6), 060901.

(30) Liu, M.; Yazdani, N.; Yarema, M.; Jansen, M.; Wood, V.; Sargent, E. H. Colloidal quantum dot electronics. *Nature Electronics* **2021**, *4* (8), 548−558.

(31) Shcherbakov-Wu, W.; Tisdale, W. A. A time-domain view of charge carriers in semiconductor nanocrystal solids. *Chemical Science* **2020**, *11* (20), 5157−5167.

(32) Lhuillier, E.; Keuleyan, S.; Rekemeyer, P.; Guyot-Sionnest, P. Thermal properties of mid-infrared colloidal quantum dot detectors. *J. Appl. Phys.* **2011**, *110* (3), 033110.

(33) Melnychuk, C.; Guyot-Sionnest, P. Thermodynamic Limits to HgTe Quantum Dot Infrared Detector Performance. *J. Electron. Mater.* **2022**, *51* (3), 1428−1435.

(34) Yazdani, N.; Andermatt, S.; Yarema, M.; Farto, V.; Bani-Hashemian, M. H.; Volk, S.; Lin, W. M. M.; Yarema, O.; Luisier, M.; Wood, V. Charge transport in semiconductors assembled from nanocrystal quantum dots. *Nat. Commun.* **2020**, *11*, 2852.

(35) Xing, Y.; Yazdani, N.; Lin, W. M. M.; Yarema, M.; Zahn, R.; Wood, V. Effect of Positional Disorders on Charge Transport in Nanocrystal Quantum Dot Thin Films. *ACS Applied Electronic Materials* **2022**, *4*, 631−642.

(36) Yang, J.; Hu, H.; Lv, Y.; Yuan, M.; Wang, B.; He, Z.; Chen, S.; Wang, Y.; Hu, Z.; Yu, M.; et al. Ligand-Engineered HgTe Colloidal Quantum Dot Solids for Infrared Photodetectors. *Nano Lett.* **2022**, *22* (8), 3465−3472.

(37) Klimov, V. I.; McGuire, J. A.; Schaller, R. D.; Rupasov, V. I. Scaling of multiexciton lifetimes in semiconductor nanocrystals. *Phys. Rev. B* **2008**, *77*, 195324.

(38) Lhuillier, E.; Keuleyan, S.; Guyot-Sionnest, P. Optical properties of HgTe colloidal quantum dots. *Nanotechnology* **2012**, *23* (17), 175705.

(39) Ackerman, M. M.; Tang, X.; Guyot-Sionnest, P. Fast and sensitive colloidal quantum dot mid-wave infrared photodetectors. *ACS Nano* **2018**, *12* (7), 7264−7271.

(40) Chen, M.; Lan, X.; Tang, X.; Wang, Y.; Hudson, M. H.; Talapin, D. V.; Guyot-Sionnest, P. High Carrier Mobility in HgTe Quantum Dot Solids Improves Mid-IR Photodetector. *ACS Photonics* **2019**, *6* (9), 2358−2365.

(41) Talapin, D. V.; Murray, C. B. PbSe nanocrystal solids for n-and p-channel thin film field-effect transistors. *Science* **2005**, *310* (5745), 86−89.

(42) Rastogi, P.; Chu, A.; Dang, T. H.; Prado, Y.; Gréboval, C.; Qu, J.; Dabard, C.; Khalili, A.; Dandeu, E.; Fix, B.; Xu, X. Z.; Ithurria, S.; Vincent, G.; Gallas, B.; Lhuillier, E. Complex optical index of HgTe nanocrystal infrared thin films and its use for short wave infrared photodiode design. *Advanced Optical Materials* **2021**, *9*, 2002066.

(43) Keuleyan, S.; Lhuillier, E.; Guyot-Sionnest, P. Synthesis of colloidal HgTe quantum dots for narrow mid-IR emission and detection. *J. Am. Chem. Soc.* **2011**, *133* (41), 16422−16424.

(44) Melnychuk, C.; Guyot-Sionnest, P. Slow Auger relaxation in HgTe colloidal quantum dots. *J. Phys. Chem. Lett.* **2018**, *9* (9), 2208−2211.

(45) Chu, A.; Gréboval, C.; Prado, Y.; Majjad, H.; Delerue, C.; Dayen, J.; Vincent, G.; Lhuillier, E. Infrared photoconduction at the diffusion length limit in HgTe nanocrystal arrays. *Nat. Commun.* **2021**, *12*, 1794.

https://doi.org/10.1021/acs.jpcc.2c05391